Chemical Science

ROYAL SOCIETY OF CHEMISTRY

EDGE ARTICLE

View Article Online
View Journal | View Issue

Cite this: *Chem. Sci.*, 2022, **13**, 5707

All publication charges for this article have been paid for by the Royal Society of Chemistry

Heme compound II models in chemoselectivity and disproportionation reactions†

Ranjana Gupta, ‡[a] Xiao-Xi Li, ‡[a] Youngseob Lee,[b] Mi Sook Seo,[a] Yong-Min Lee,[a] Sachiko Yanagisawa,[c] Minoru Kubo,[c] Ritimukta Sarangi,*[d] Kyung-Bin Cho,*[b] Shunichi Fukuzumi*[a] and Wonwoo Nam*[a]

Received 1st March 2022
Accepted 11th April 2022

DOI: 10.1039/d2sc01232d

rsc.li/chemical-science

Heme compound II models bearing electron-deficient and -rich porphyrins, $[Fe^{IV}(O)(TPFPP)(Cl)]^-$ (**1a**) and $[Fe^{IV}(O)(TMP)(Cl)]^-$ (**2a**), respectively, are synthesized, spectroscopically characterized, and investigated in chemoselectivity and disproportionation reactions using cyclohexene as a mechanistic probe. Interestingly, cyclohexene oxidation by **1a** occurs at the allylic C–H bonds with a high kinetic isotope effect (KIE) of 41, yielding 2-cyclohexen-1-ol product; this chemoselectivity is the same as that of nonheme iron(IV)-oxo intermediates. In contrast, as observed in heme compound I models, **2a** yields cyclohexene oxide product with a KIE of 1, demonstrating a preference for C=C epoxidation. The latter result is interpreted as **2a** disproportionating to form $[Fe^{IV}(O)(TMP^{+\bullet})]^+$ (**2b**) and $Fe^{III}(OH)(TMP)$, and **2b** becoming the active oxidant to conduct the cyclohexene epoxidation. In contrast to **2a**, **1a** does not disproportionate under the present reaction conditions. DFT calculations confirm that compound II models prefer C–H bond hydroxylation and that disproportionation of compound II models is controlled thermodynamically by the porphyrin ligands. Other aspects, such as acid and base effects on the disproportionation of compound II models, have been discussed as well.

Introduction

Heme enzymes, such as cytochromes P450 (CYP 450), utilize high-valent iron(IV)-oxo porphyrin π-cation radical intermediates, referred to as compound I (Cpd I) and two oxidizing equivalents above the resting ferric state, to achieve highly efficient and selective oxidation reactions, such as in alkane hydroxylation and olefin epoxidation.[1] In biomimetic studies, a number of synthetic Cpd I models have been synthesized and characterized with various spectroscopic techniques, and their reactivities have been investigated intensively in various oxidation reactions.[2] In contrast, high-valent iron(IV)-oxo porphyrin intermediates, referred to as compound II (Cpd II) and one oxidizing equivalent above the resting ferric state, have been investigated less intensively in enzymatic and biomimetic reactions, since they are not the key active oxidants in enzymatic reactions and their reactivities are low compared to the strong oxidizing power of Cpd I intermediates.[3] Therefore, the chemistry of Cpd II models still remains elusive in biomimetic oxidation reactions, although an elegant study on the acid-catalyzed disproportionation reaction of Cpd II models to Cpd I and iron(III) porphyrin complexes has been reported by Fujii and co-workers very recently.[4]

Iron(IV)-oxo intermediates have also been trapped and characterized in nonheme iron enzymes.[5] In biomimetic studies, since the first crystal structure of a synthetic nonheme iron(IV)-oxo complex, $[(TMC)Fe^{IV}(O)(MeCN)]^{2+}$ (TMC = 1,4,8,11-tetramethyl-1,4,8,11-tetraazacyclotetradecane), was reported in 2003,[6] a large number (>80) of nonheme iron(IV)-oxo complexes have been synthesized and characterized spectroscopically and/or structurally and their reactivities have been extensively investigated in various oxidation reactions, such as hydrogen atom transfer (HAT) and oxygen atom transfer (OAT) reactions;[7] some of the nonheme iron(IV)-oxo complexes have shown reactivities similar to Cpd I models in the oxidation of organic substrates with a strong oxidizing power.[8] However, in a couple of reactions, the reactivities and mechanisms of the nonheme iron(IV)-oxo complexes were shown to be different from those of Cpd I models.[9,10a] One example is the different chemoselectivities observed in the oxidation of cyclohexene by Cpd I models and nonheme iron(IV)-oxo complexes; Cpd I models afford cyclohexene oxide as the product,[11] whereas nonheme

[a]*Department of Chemistry and Nano Science, Ewha Womans University, Seoul 03760, Korea. E-mail: fukuzumi@chem.eng.osaka-u.ac.jp; wwnam@ewha.ac.kr*

[b]*Department of Chemistry, Jeonbuk National University, Jeonju, 54896, Korea. E-mail: workforkyung@jbnu.ac.kr*

[c]*Graduate School of Life Science, University of Hyogo, Hyogo, 678-1297, Japan*

[d]*Stanford Synchrotron Radiation Lightsource, SLAC National Accelerator Laboratory, Stanford University, California, 94023, USA. E-mail: ritis@slac.stanford.edu*

† Electronic supplementary information (ESI) available: Experimental section, Fig. S1–S19 for spectroscopic characterization and kinetic data, Tables S1–S5 and Fig. S20 for EXAFS and DFT calculation results, and calculated Cartesian coordinates. See https://doi.org/10.1039/d2sc01232d

‡ These authors contributed equally.

iron(IV)-oxo complexes prefer allylic C–H bond hydroxylation to C=C bond epoxidation (see Scheme 1B).[10a] The distinct chemoselectivity shown by nonheme metal(IV)-oxo complexes was interpreted with density functional theory (DFT) calculations.[10]

As mentioned above, the chemistry of Cpd II models, iron(IV)-oxo porphyrin complexes, has been explored less intensively in oxidation reactions, compared to the well-studied Cpd I models and nonheme iron(IV)-oxo complexes. For example, while the electronic effect of porphyrin ligands, such as electron-rich *versus* electron-deficient porphyrins, has been well addressed in Cpd I models,[11b,12,13] the porphyrin ligand effect(s) of Cpd II models in oxidation reactions has rarely been discussed. Also, the effect(s) of heme and nonheme ligands on the reactivities of iron(IV)-oxo complexes in oxidation reactions has rarely been compared. We therefore decided to investigate the reactivities of Cpd II models bearing electron-rich and -deficient porphyrins in the oxidation of cyclohexene; cyclohexene was chosen as a mechanistic probe to compare the chemoselectivity of Cpd II models to those of nonheme iron(IV)-oxo complexes (*i.e.*, the effect of heme *vs.* nonheme ligands on the chemoselectivity of iron(IV)-oxo species) and Cpd I models (*i.e.*, the chemoselectivity of Cpd I *vs.* Cpd II in heme systems) (Scheme 1B and C).[10,11]

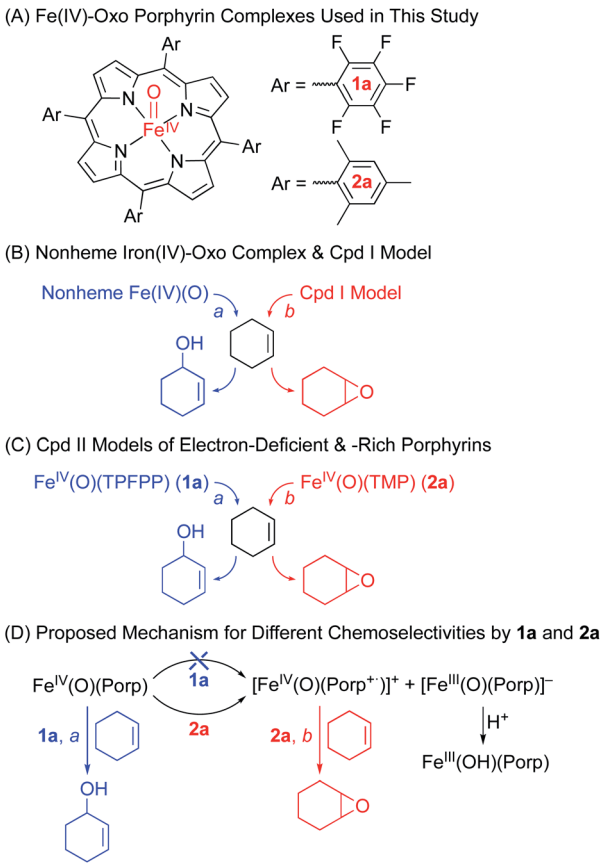

Scheme 1 (A) Structures of Cpd II models, **1a** and **2a**. (B) Chemoselectivities of nonheme iron(IV)-oxo and Cpd I complexes. (C) Chemoselectivities of Cpd II models with electron-deficient and -rich porphyrins. (D) Proposed mechanism for the different chemoselectivities of **1a** and **2a**.

We now report that the chemoselectivity of Cpd II models in the oxidation of cyclohexene varies depending on the electron-richness of the porphyrin ligands (see Scheme 1A for structures); that is, a Cpd II model with an electron-deficient porphyrin ligand, $[Fe^{IV}(O)(TPFPP)(Cl)]^-$ (**1a**, TPFPP = *meso*-tetrakis(pentafluorophenyl)porphyrinato dianion), affords the allylic oxidation product, as observed in the reactions of nonheme iron(IV)-oxo complexes (see Scheme 1B and C, reaction pathway a),[10] whereas a Cpd II model with an electron-rich porphyrin ligand, $[Fe^{IV}(O)(TMP)(Cl)]^-$ (**2a**, TMP = *meso*-tetrakis(2,4,6-trimethylphenyl)porphyrinato dianion), yields the cyclohexene oxide product, as observed in the Cpd I model reactions (see Scheme 1B and C, reaction pathway b).[11] We also report that the preference for C=C bond epoxidation by **2a** results from the disproportionation of **2a** that forms Cpd I, $[Fe^{IV}(O)(TMP^{+\cdot})]^+$ (**2b**), as the active oxidant that effects the epoxidation of cyclohexene to give the corresponding epoxide product selectively (see Scheme 1D, reaction pathway b). In contrast to **2a**, the disproportionation of **1a** does not occur under the reaction conditions and **1a** abstracts a hydrogen atom (H-atom) from the allylic C–H bonds to give the allylic oxidation product (see Scheme 1D, reaction pathway a). The different chemoselectivities shown by **1a** and **2a** are then interpreted with DFT calculations. Other mechanistic aspects, such as the effects of acid and base on the disproportionation of Cpd II models (**1a** and **2a**) and the reactivities of Cpd I models (*i.e.*, **1b** and **2b**) in oxidation reactions, have been discussed as well.

Results and discussion

Synthesis of $[Fe^{IV}(O)(TPFPP)(Cl)]^-$ (1a)

The iron(IV)-oxo porphyrin complex, $[Fe^{IV}(O)(TPFPP)(Cl)]^-$ (**1a**), was synthesized by reacting $Fe^{III}(TPFPP)(Cl)$ (**1**) with 4.0 equiv. of *meta*-chloroperbenzoic acid (*m*-CPBA) in acetonitrile (MeCN, 2 mL) containing H_2O (15 μL) at 283 K; the colour of the reaction solution changed from brown to red and **1a** was formed within 2 min (see Fig. 1a for the electronic absorption spectral change in the Q-band region; also see Fig. S1† for the full range of spectra including the Soret band). **1a** was also synthesized by reacting **1** with 4.0 equiv. of iodosylbenzene (PhIO, dissolved in 50 μL of MeOH) (Fig. S2†). **1a** was stable at 233 K, allowing us to characterize it using various spectroscopic techniques, such as cold spray time-of-flight mass spectrometry (CSI-MS), electron paramagnetic resonance (EPR), resonance Raman (rRaman), and X-ray absorption spectroscopy/extended X-ray absorption fine structure (XAS/EXAFS).

First, the CSI-MS of **1a** in positive mode exhibits a prominent ion peak at a mass-to-charge ratio (*m*/*z*) of 1108.1 with mass and isotope distribution patterns corresponding to $[Fe^{IV}(^{16}O)(TPFPP)(MeCN)(Na)]^+$ (calcd *m*/*z* = 1108.0) (Fig. 1b). When **1a** was generated using $PhI^{18}O$ (prepared in 50 μL of MeOH containing 15 μL of $H_2{}^{18}O$), a two-mass unit shift from 1108.1 $\{[Fe^{IV}(^{16}O)(TPFPP)(MeCN)(Na)]^+\}$ to 1110.1 $\{[Fe^{IV}(^{18}O)(TPFPP)(MeCN)(Na)]^+\}$ was observed (Fig. 1b, inset). This CSI-MS result indicates that **1a** contains one oxygen atom. The X-band EPR spectrum of **1a** was silent, suggesting an Fe(IV) oxidation state (Fig. S3†). The rRaman spectrum of **1a**,

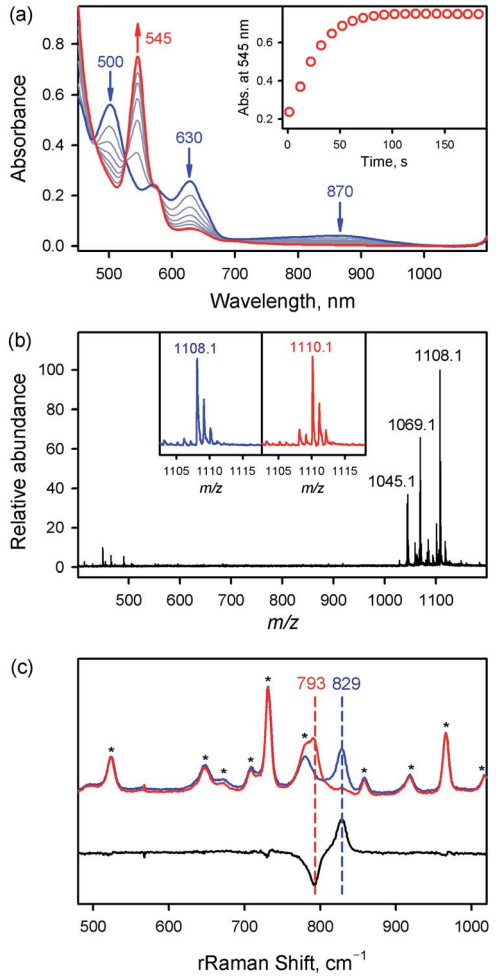

Fig. 1 (a) UV-vis spectra of Fe^{III}(TPFPP)(Cl) (**1**, blue line) and $[Fe^{IV}(O)(TPFPP)(Cl)]^-$ (**1a**, red line); **1a** was synthesized by reacting **1** (0.50 mM) with 4.0 equiv. of *m*-CPBA (2.0 mM) in MeCN at 283 K. Inset shows the time trace monitored at 545 nm due to **1a**. (b) CSI-MS spectrum of **1a**. The peaks at m/z = 1045.1, 1069.1, and 1108.1 correspond to $[Fe^{IV}(O)(TPFPP)(H)]^+$ (calcd m/z = 1045.0), $[Fe^{III}(TPFPP)(MeCN)]^+$ (calcd m/z = 1069.0), and $[Fe^{IV}(O)(TPFPP)(MeCN)(Na)]^+$ (calcd m/z = 1108.0), respectively. Insets show the observed isotope distribution patterns for **1a**-^{16}O (blue line) and **1a**-^{18}O (red line); **1a**-^{16}O and **1a**-^{18}O were prepared by reacting **1** (0.10 mM) with $PhI^{16}O$ (0.40 mM) and $PhI^{18}O$ (0.40 mM), respectively, in MeCN at 233 K. (c) Resonance Raman spectra of **1a**-^{16}O (blue line) and **1a**-^{18}O (red line) obtained upon excitation at 405 nm. The black line is the difference spectrum of **1a**-^{16}O and **1a**-^{18}O; **1a**-^{16}O and **1a**-^{18}O were prepared by reacting **1** (1.0 mM) with $PhI^{16}O$ (4.0 mM) and $PhI^{18}O$ (4.0 mM), respectively, in MeCN at 233 K. The peaks marked with an asterisk originated from the solvent.

measured upon 405 nm excitation at 233 K, displayed one isotopically sensitive band at 829 cm^{-1}, which shifted to 793 cm^{-1} upon ^{18}O-substitution (Fig. 1c). The observed isotopic shift of −36 cm^{-1} with ^{18}O-substitution is in good agreement with the calculated value for a diatomic Fe–O oscillator (−37 cm^{-1}). The rRaman data indicate that **1a** possesses an Fe=O unit, as reported in Cpd I, Cpd II, and nonheme iron(IV)-oxo species.[14,15]

Fe K-edge XAS and EXAFS data for **1** and **1a** are presented in Fig. 2 (see also Table S1 and Fig. S4†). The rising-edge energy position at half maxima shifts from 7123.6 eV to 7124.3 eV, indicating an increase in oxidation state on going from **1** (Fe^{III}) to **1a** (Fe^{IV}). The pre-edge region, which represents the electric dipole forbidden, quadrupole allowed 1s → 3d transition, shows a dramatic increase in intensity in **1a** relative to **1**.[16] This is characteristic of a short bond (*i.e.*, Fe=O) along the molecular *z*-axis, which enhances Fe $3d_{z^2}$–$4p_z$ mixing, leading to the enhancement of dipole allowed character into the pre-edge feature. In contrast, the longer Fe–Cl bond in **1** disallows strong mixing and the pre-edge intensity remains modest. A qualitative comparison of the EXAFS data (Fig. 2b) shows a significant phase shift, indicating a large structural change between **1** and **1a**. FEFF fits to the data for **1a** are consistent with 1 Fe–O at 1.65 Å, 4 Fe–N at 2.00 Å, and 1 Fe–Cl at 2.24 Å. The second and third shells were fitted with single and multiple scattering contributions from the TPFPP ligand. Therefore, the data are consistent with the formation of an Fe(IV)=O species with a short 1.65 Å Fe–O bond distance.

Synthesis of $[Fe^{IV}(O)(TMP)(Cl)]^-$ (2a)

When 3.0 equiv. of PhIO, dissolved in 50 μL of MeOH, was added to a solution of Fe^{III}(TMP)(Cl) (**2**) in butyronitrile at 253 K, the formation of an iron(IV)-oxo porphyrin complex, $[Fe^{IV}(O)(TMP)(Cl)]^-$ (**2a**), was observed within 10 min (see Fig. S5a† for the electronic absorption spectral change in the Q-band region; also see Fig. S5b† for the full range of spectra including the Soret band). The X-band EPR spectrum of **2a** was

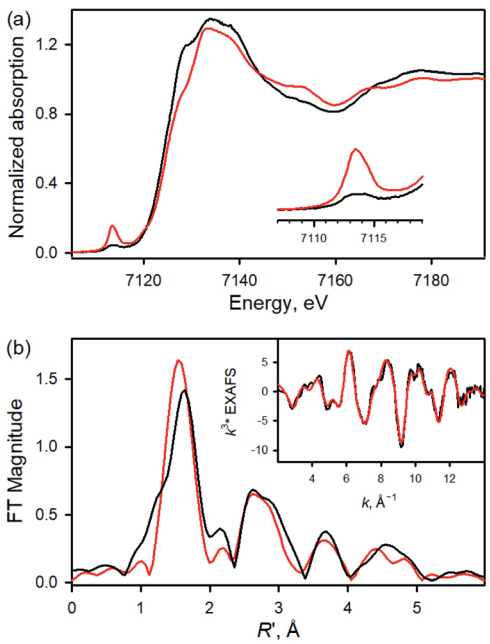

Fig. 2 (a) Normalized Fe K-edge XAS data for Fe^{III}(TPFPP)(Cl) (**1**, black line) and $[Fe^{IV}(O)(TPFPP)(Cl)]^-$ (**1a**, red line). Inset shows the expanded pre-edge region. (b) Comparison of the nonphase-shift-corrected Fourier transform (FT) data for **1** (black line) and **1a** (red line). Inset shows the EXAFS data for **1a** (black line) and fit (red line).

silent, suggesting an Fe(IV) oxidation state (Fig. S6†). The rRaman spectrum of **2a**, measured upon 442 nm excitation at 218 K, displayed one isotopically sensitive band at 828 cm^{-1}, which shifted to 791 cm^{-1} upon ^{18}O-substitution (Fig. S7†). The observed isotopic shift of −37 cm^{-1} with ^{18}O-substitution is in good agreement with the calculated value for a diatomic Fe–O oscillator (−37 cm^{-1}). The rRaman data indicate that **2a** possesses an Fe=O unit.[14,15] Based on the spectroscopic characterization presented above, we have confirmed that iron(IV)-oxo complexes bearing electron-deficient and -rich porphyrin ligands, **1a** and **2a**, were successfully synthesized for further reactivity studies.

Cyclohexene oxidation by 1a and 2a

We then investigated the reactivities of **1a** and **2a** in cyclohexene oxidation. Since **1a** reacted slowly with cyclohexene in MeCN at 253 K, the reactivity of **1a** with cyclohexene was investigated at 283 K. Upon addition of cyclohexene to the reaction solution of **1a**, the electronic absorption band at 545 nm corresponding to **1a** disappeared with the concomitant formation of bands at 500 and 630 nm corresponding to the starting $[Fe^{III}(TPFPP)]^+$ complex with clear isosbestic points at 470, 523, and 564 nm (Fig. 3a). The decay rate of **1a** obeyed first-order kinetics (Fig. 3a, insets) and increased linearly with an increase in the concentration of cyclohexene, affording a second-order rate constant of $k_{2(H)} = 6.1 \times 10^{-3}$ M^{-1} s^{-1} at 283 K (Fig. 3b, blue line). The second-order rate constant determined in the oxidation of deuterated cyclohexene (cyclohexene-d_{10}) by **1a** was $k_{2(D)} = 1.5 \times 10^{-4}$ M^{-1} s^{-1} (Fig. 3b, red line), giving a large kinetic isotope effect (KIE) value of 41. Product analysis of the reaction solution revealed the formation of 2-cyclohexen-1-ol as a major product in the oxidation of cyclohexene by **1a** (85% yield based on the amount of **1a** used). Also, the oxygen atom in the 2-cyclohexen-1-ol product was found to derive from the oxidant by carrying out ^{18}O-labeling experiments with **1a**-^{18}O; the ^{18}O-percent in the 2-cyclohexen-1-ol product was ~75% (Fig. S8†). The formation of 2-cyclohexen-1-ol with the large KIE value of 41 demonstrates that the allylic C–H bond oxidation pathway is preferred over the C=C bond epoxidation pathway in the oxidation of cyclohexene by **1a** (Scheme 1C, pathway a); the preference for C–H bond hydroxylation in cyclohexene oxidation was observed in nonheme iron(IV)-oxo and other nonheme metal(IV)-oxo complexes.[10] In addition, the decay product of **1a** was found to be $[Fe^{III}(TPFPP)]^+$ by UV-vis and EPR spectroscopies (Fig. 3a and S9†); it is noted that nonheme iron(IV)-oxo species are converted to iron(III) species in C–H bond hydroxylation reactions.[9,10]

Interestingly, the reactivity of **2a** bearing an electron-rich porphyrin ligand was greater than that of **1a** bearing an electron-deficient porphyrin ligand (Scheme 2, reaction 1); therefore, the reaction of **2a** and cyclohexene was carried out at 253 K, which is lower than the reaction temperature for **1a** (*e.g.*, 283 K). Upon addition of cyclohexene to the reaction solution of **2a**, the electronic absorption band at 545 nm corresponding to **2a** disappeared with the concurrent formation of bands at 505 and 575 nm corresponding to the starting $[Fe^{III}(TMP)]^+$ complex with clear isosbestic points at 465, 527, 585, and 710 nm (Fig. S10†). Surprisingly, the reaction was found to obey second-order kinetics, as shown in Fig. 4a (Scheme 2, reaction 2); it is noted that the reaction of **1a** and cyclohexene followed first-order kinetics (Fig. 3a). The observed rate constant (k_{obs}) of **2a** increased with an increase in the concentration of cyclohexene, but a saturation plot was obtained at high concentrations of cyclohexene (Fig. 4b); the observation of saturation behavior suggests that there is a relatively fast equilibrium that precedes the oxygen atom transfer reaction (*vide infra*).[17] The latter result is also distinct from the observation of good linear correlation between the rate constant and the cyclohexene concentration in

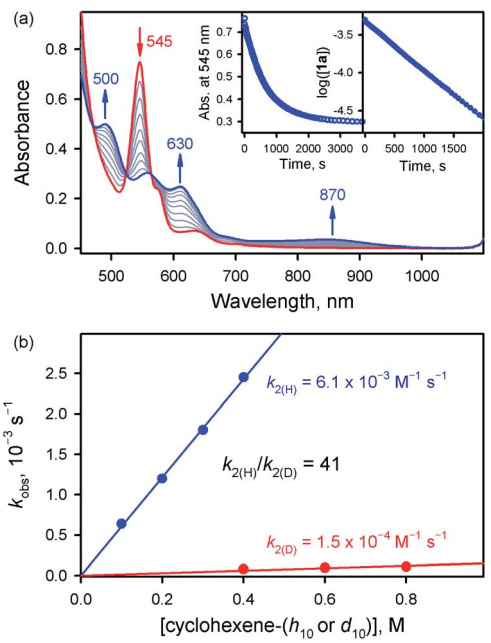

Fig. 3 (a) UV-vis absorption spectral changes observed in the reaction of **1a** (0.50 mM) and cyclohexene (100 mM) in MeCN at 283 K. Insets show the time profile of the absorbance change at 545 nm (left panel) and the first-order plot of log([**1a**]) *vs.* time (right panel). (b) Plots of the pseudo-first-order rate constants (k_{obs}) against the concentration of cyclohexene-h_{10} (blue circles) and cyclohexene-d_{10} (red circles) to determine k_2 values in MeCN at 283 K.

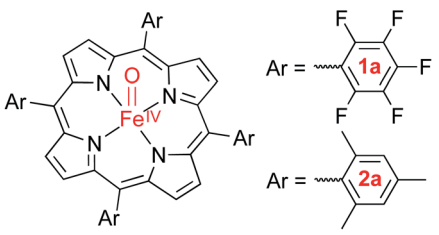

1. Reactivity of **1a** < **2a**
2. First-order kinetics for **1a** vs second-order kinetics for **2a**
3. Linear correlation for **1a** vs saturation behavior for **2a** against substrate concentration
4. KIE values of 41 for **1a** vs 1.0 for **2a**
5. 2-Cyclohexen-1-ol for **1a** vs cyclohexene oxide for **2a**

Scheme 2 Observed reactivities of **1a** and **2a**.

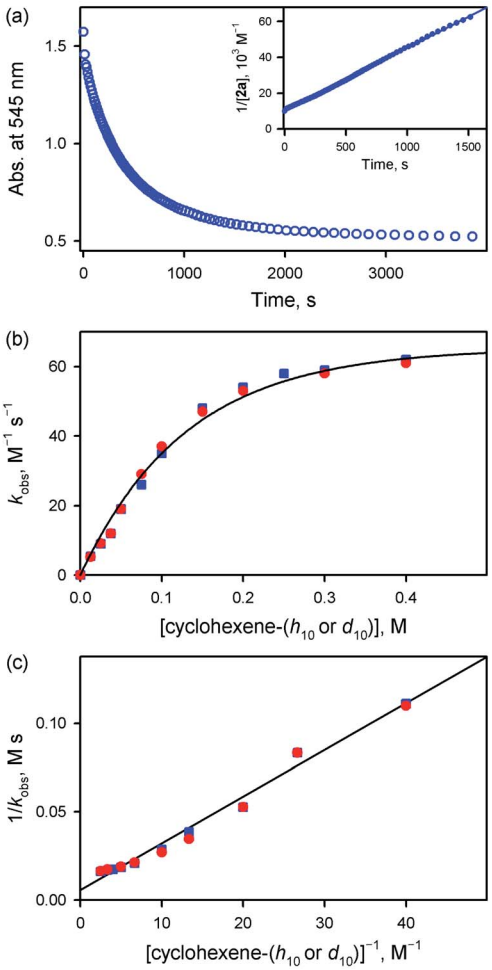

Fig. 4 (a) Time profile of the absorbance change at 545 nm due to the decay of **2a** (0.10 mM) in the reaction of **2a** with cyclohexene (100 mM) in butyronitrile at 253 K. Inset shows the second-order plot of 1/[**2a**] *vs.* time. (b) Plots of the observed second-order rate constants (k_{obs}) against concentrations of cyclohexene-h_{10} (blue squares) and cyclohexene-d_{10} (red circles) obtained in the reactions of **2a** (0.10 mM) with cyclohexene-h_{10} and cyclohexene-d_{10} in butyronitrile at 253 K, respectively. (c) Plots of k_{obs}^{-1} *vs.* [cyclohexene-h_{10}]$^{-1}$ (blue squares) and [cyclohexene-d_{10}]$^{-1}$ (red circles) obtained in the reactions of **2a** (0.10 mM) with cyclohexene-h_{10} and cyclohexene-d_{10} in butyronitrile at 253 K, respectively.

the reaction of **1a** and cyclohexene (Fig. 3b) (Scheme 2, reaction 3). When cyclohexene-h_{10} was replaced by cyclohexene-d_{10} in the oxidation reaction by **2a**, the reaction exhibited second-order kinetics, saturation behavior, and a KIE value of 1.0 (Fig. 4b and c). It is of interest to note that the KIEs determined in the reactions of **1a** and **2a** are very different: 41 for **1a** and 1.0 for **2a** (Scheme 2, reaction 4) (*vide infra*).[18]

Product analysis of the reaction solution of **2a** and cyclohexene revealed the formation of cyclohexene oxide as the sole product (~50% based on the concentration of **2a**) (Scheme 1C, pathway b), which is very different from the 2-cyclohexen-1-ol produced in the reaction of **1a** and cyclohexene (Scheme 1C, pathway a) (see also Scheme 2, reaction 5); it is noted that the reactions of Cpd I models and cyclohexene afford the cyclohexene oxide product (Scheme 1B, pathway b).[11] The source of oxygen atoms in the cyclohexene oxide product was found to derive from the oxidant by carrying out ^{18}O-labeling experiments with **2a**-^{18}O; the ^{18}O-percent in the cyclohexene oxide product was >85% (Fig. S11†). In addition to the UV-vis spectrum of the reaction solution (Fig. S10†), the decay product of **2a** was confirmed to be [Fe^{III}(TMP)]$^+$ by EPR spectroscopy (Fig. S12†). As a conclusion, we have shown that the reaction of **1a** and cyclohexene prefers allylic C–H bond oxidation to give 2-cyclohexen-1-ol (Scheme 1C, pathway a), whereas the reaction of **2a** and cyclohexene favors C=C bond epoxidation and cyclohexene oxide is the product (Scheme 1C, pathway b). Further, it is notable that the reaction of **1a** resembles the mononuclear nonheme iron(IV)-oxo reaction (*i.e.*, C–H bond hydroxylation; Scheme 1B, pathway a),[10] whereas the reaction of **2a** follows the Cpd I reaction (*i.e.*, C=C bond epoxidation; Scheme 1B, pathway b).[11]

Disproportionation of Cpd II to Cpd I and [Fe^{III}(Porp)]$^+$

Why are the reactions of **1a** and **2a** very different in the oxidation of cyclohexene, such as the preference for C–H bond hydroxylation with a large KIE value *vs.* C=C bond epoxidation with a KIE value of 1.0, first-order kinetics *vs.* second-order kinetics, and no saturation behavior *vs.* saturation behavior (see Scheme 2)? These differences are rationalized by disproportionation of **2a** (Scheme 1D, reaction pathway of **2a**), but not **1a** (Scheme 1D, reaction pathway of **1a**). That is, in the reaction of **2a**, the second-order kinetics together with the saturation plot of k_{obs} *vs.* concentration of cyclohexene and the absence of a kinetic isotope effect can be well explained by the disproportionation of [Fe^{IV}(O)(TMP)(Cl)]$^-$ (**2a**) to afford [Fe^{IV}(O)(TMP$^{+\bullet}$)]$^+$ (**2b**), which is the active oxidant that epoxidizes cyclohexene to give the corresponding epoxide product (Scheme 3). According to Scheme 3, the rate of disappearance of **2a** is given by eqn (1),

$$d[\mathbf{2a}]/dt = -k_1[\mathbf{2a}]^2 + k_{-1}[C] \quad (1)$$

where C is a pair of [Fe^{IV}(O)(TMP$^{+\bullet}$)]$^+$ and Fe^{III}(OH)(TMP), as shown in Scheme 3. The formation rate of C is given by eqn (2), where [S] is the substrate concentration, [cyclohexene]. Eqn (3) is derived from eqn (1) and (2).

$$d[C]/dt = k_1[\mathbf{2a}]^2 - k_{-1}[C] - k_{ox}[C][S] \quad (2)$$

$$d([\mathbf{2a}] + [C])/dt = -k_{ox}[C][S] \quad (3)$$

Since no [Fe^{IV}(O)(TMP$^{+\bullet}$)]$^+$ was observed, [C] ≪ [**2a**]. Under such conditions, eqn (3) is rewritten as eqn (4).

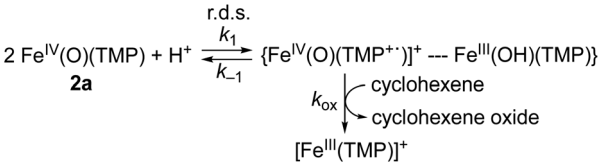

Scheme 3 Disproportionation reaction of **2a**.

Table 1 Rate constants of the oxidation of cyclohexene-h_{10} and cyclohexene-d_{10} (see the column of $k_{ox}K_1$) and the disproportionation (see the column of k_1) of **2a** in butyronitrile at 253 K

Substrate	$k_{ox}K_1$, M^{-2} s^{-1}	k_1, M^{-1} s^{-1}
Cyclohexene-h_{10}	3.8×10^2	1.9×10^2
Cyclohexene-d_{10}	3.8×10^2	1.9×10^2

$$d[\mathbf{2a}]/dt = -k_{ox}[C][S] \quad (4)$$

By applying the steady-state approximation ($d[C]/dt \approx 0$), eqn (5) is obtained from eqn (2). Thus, eqn (6) is obtained from eqn (4) and (5), which fits the second-order kinetics for the disappearance of **2a**. The observed second-order constant (k_{obs}) is given by eqn (7), which can be converted to a linear correlation between k_{obs}^{-1} and $[S]^{-1}$ [eqn (8)].

$$[C] = k_1[\mathbf{2a}]^2/(k_{-1} + k_{ox}[S]) \quad (5)$$

$$d[\mathbf{2a}]/dt = -k_1k_{ox}[\mathbf{2a}]^2[S]/(k_{-1} + k_{ox}[S]) \quad (6)$$

$$k_{obs} = k_1k_{ox}[S]/(k_{-1} + k_{ox}[S]) \quad (7)$$

$$k_{obs}^{-1} = (k_{-1}/k_1k_{ox})[S]^{-1} + (k_1)^{-1} \quad (8)$$

Such a linear correlation is confirmed in a plot of k_{obs}^{-1} *vs.* $[\text{cyclohexene}]^{-1}$ in Fig. 4c. The intercept corresponds to the disproportionation rate constant (k_1^{-1}) and the slope corresponds to $k_{-1}/(k_1k_{ox})$. As expected, no KIE was observed for k_1 (Fig. 4c and Table 1). The k_1 and $k_{ox}K_1$ ($K_1 = k_1/k_{-1}$) values are summarized in Table 1.

We therefore conclude that the disproportionation of **1a** bearing an electron-deficient porphyrin ligand does not occur under the reaction conditions, whereas **2a** bearing an electron-rich porphyrin ligand is disproportionated to form an iron(IV)-oxo porphyrin π-cation radical species, $[Fe^{IV}(O)(TMP^{+\bullet})]^+$ (**2b**), as an active oxidant. This is the reason why **1a** and **2a** exhibited different reactivities in the oxidation of cyclohexene, as summarized in Scheme 2; that is, **1a** abstracts a hydrogen atom from allylic C–H bonds, whereas **2a** is disproportionated to **2b** that epoxidizes cyclohexene to give cyclohexene oxide selectively (Scheme 1D).

Although the disproportionation reactions of high-valent metal-oxo (and metal-imido) complexes in the presence of protons have been well addressed previously,[19–21] we report an example showing that the disproportionation reaction can be modulated by the electron-richness of porphyrin ligands and that the different reactivities of iron(IV)-oxo porphyrin complexes, **1a** and **2a** result from the disproportionation reaction by **2a**, but not by **1a**. Further, the present study demonstrates that iron(IV)-oxo porphyrins prefer C–H bond hydroxylation to C=C bond epoxidation, as reported in nonheme iron(IV)-oxo (and other metal(IV)-oxo) systems.[10]

Cyclohexene oxidation by 1b and 2b

In order to prove the possibility of the disproportionation reaction of **2a**, but not **1a**, and the formation of iron(IV)-oxo porphyrin π-cation radical species as an active oxidant in the cyclohexene oxidation by **2a**, but not by **1a** (Schemes 1D and 3), we synthesized iron(IV)-oxo porphyrin π-cation radical species independently, $[Fe^{IV}(O)(TPFPP^{+\bullet})]^+$ (**1b**) and $[Fe^{IV}(O)(TMP^{+\bullet})]^+$ (**2b**), investigated their reactivities with cyclohexene, and compared the reactivities of **1b** and **2b** to those of **1a** and **2a**. First, the addition of 4.0 equiv. of *m*-CPBA to $[Fe^{III}(TPFPP)](OTf)$ ($OTf = CF_3SO_3^-$) and $[Fe^{III}(TMP)]Cl$ led to the formation of $[Fe^{IV}(O)(TPFPP^{+\bullet})]^+$ (**1b**) and $[Fe^{IV}(O)(TMP^{+\bullet})]^+$ (**2b**), respectively (Fig. S13†).[3c,11–13,22] Then, the reactivities of **1b** and **2b** were investigated in cyclohexene oxidation. Upon the addition of cyclohexene-h_{10} to a CH_2Cl_2 solution of **1b** at 213 K, the absorption band at 660 nm due to **1b** disappeared and absorption bands corresponding to $[Fe^{III}(TPFPP)]^+$ appeared concurrently (Fig. S14†). The second-order rate constant, $k_{2(H)}$, was determined to be 1.4×10^4 M^{-1} s^{-1} at 213 K (Fig. S15†). Similarly, the second-order rate constant in the oxidation of cyclohexene-d_{10} by **1b** was determined to be $k_{2(D)} = 1.4 \times 10^4$ M^{-1} s^{-1} (Fig. S15†), giving a KIE value of 1.0. Organic product analysis revealed that cyclohexene oxide, but no allylic oxidation products, was formed as a product. The observations of the KIE of 1.0 and the cyclohexene oxide product in the reaction of **1b** and cyclohexene were different from the results obtained in the reaction of **1a** and cyclohexene, such as the KIE value of 41 and the formation of the allylic oxidation product in the latter reaction. Based on the reactivity comparison of **1a** and the *in situ* generated iron(IV)-oxo porphyrin π-cation radical species, $[Fe^{IV}(O)(TPFPP^{+\bullet})]^+$ (**1b**), we conclude that the disproportionation of **1a** does not occur to form **1b** (*vide infra*) and that **1a**, but not **1b**, is the active oxidant that oxidizes cyclohexene to give the 2-cyclohexen-1-ol product (Scheme 1D, pathway a).

Similarly, upon the addition of cyclohexene-h_{10} to a butyronitrile solution of $[Fe^{IV}(O)(TMP^{+\bullet})]^+$ (**2b**), the absorption band at 666 nm corresponding to **2b** disappeared with the concurrent formation of an absorption band at 505 nm corresponding to $[Fe^{III}(TMP)]^+$ (Fig. S16†). From the slope of a linear correlation of the pseudo-first-order rate constants *vs.* concentration of cyclohexene, the second-order rate constant was determined to be $k_{2(H)} = 21$ M^{-1} s^{-1} in butyronitrile at 253 K (Fig. S17†). Also, the second-order rate constant in the oxidation of deuterated cyclohexene (cyclohexene-d_{10}) by **2b** was determined to be $k_{2(D)} = 21$ M^{-1} s^{-1} (Fig. S17†), giving a KIE value of 1.0. Organic product analysis revealed the formation of cyclohexene oxide without the allylic oxidation product (*e.g.*, 2-cyclohexen-1-ol). Thus, the reactivity of **2b** was found to be the same as that of **2a** in cyclohexene oxidation, such as the KIE of 1.0 and the cyclohexene oxide product. Conclusively, these results confirm that the active oxidant in the reaction of **2a** and cyclohexene is not **2a** but **2b**, which is formed *via* a disproportionation reaction of **2a** (Scheme 1D, pathway b and Scheme 3).

Effects of acid and base on the reactions of 1a and 2a

To investigate further this unusual behavior of Cpd II models in the oxidation of cyclohexene, such as the preference for C–H bond hydroxylation *vs.* C=C bond epoxidation by **1a** and **2a**, respectively, we investigated the effects of acid and base on the

reactions of **1a** and **2a** with cyclohexene. According to Scheme 3, the disproportionation step should be affected by the proton concentration and the rate should increase with an increase in the concentration of protons.[4,19] This was confirmed by showing that the k_{obs} values of **2a** increased with an increase in the concentration of acetic acid (AcOH) (Fig. S18†). In contrast, such an acid concentration effect was not observed in the reaction of **1a** and cyclohexene upon the addition of AcOH up to 100 mM (Fig. S19†).

On the other hand, the addition of a base, such as tetramethylammonium hydroxide (TMAH), to the solution of **2a** reduced the reaction rate of **2a** (Fig. 5). In addition, interestingly, the decay of **2a** came to obey first-order kinetics (Fig. 5a). Moreover, the pseudo-first-order rate constants increased linearly with an increase in cyclohexene concentration, affording the second-order rate constant of $k_2 = 7.8 \times 10^{-4}$ M^{-1} s^{-1} in the presence of 0.25 mM TMAH (Fig. 5b). Also, product analysis of the reaction solution revealed the formation of 2-cyclohexen-1-ol product. These results, such as the first-order kinetics, the linear correlation against substrate concentration, and the formation of 2-cyclohexen-1-ol product, are in sharp contrast to those results obtained in the reactions of **2a** and cyclohexene carried out in the absence of a base, such as the second-order kinetics, the saturation behavior with substrate concentration, and the formation of cyclohexene oxide. This base effect is rationalized by the change in the mechanism in the presence of a base, such as the equilibrium shift towards the inhibition of the disproportionation of **2a** in the presence of a base (Scheme 3). Thus, our conclusion is that the active oxidant is **2a** (*e.g.*, $[Fe^{IV}(O)(TMP)]$), not **2b** (*e.g.*, $[Fe^{IV}(O)(TMP^{+\bullet})]^{+}$), in the presence of a base, showing reactivity patterns similar to those observed in the reactions of **1a** with cyclohexene (see Scheme 2).

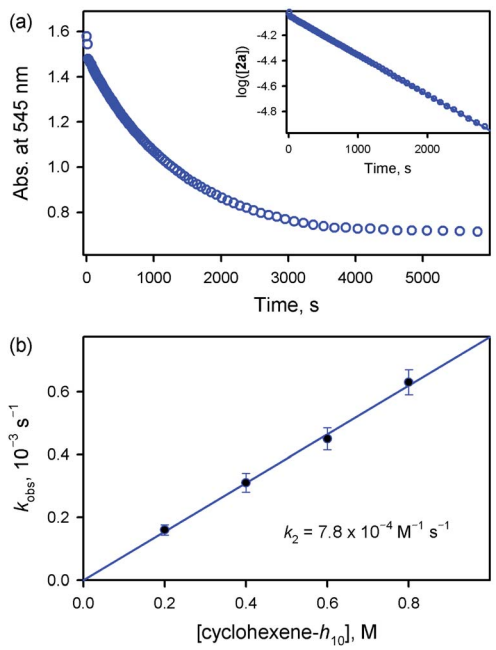

Fig. 5 (a) Time profile of the absorbance change at 545 nm due to **1a** observed in the reaction of **2a** (0.10 mM) with cyclohexene (400 mM) in the presence of TMAH (0.25 mM) in butyronitrile at 253 K. Inset shows the first-order plot of log([**2a**]) *vs.* time. (b) Plot of pseudo-first-order rate constant (k_{obs}) against the concentration of cyclohexene-h_{10} to determine the k_2 value for the reaction of **2a** and cyclohexene in the presence of TMAH (0.25 mM) in butyronitrile at 253 K.

Density functional theory (DFT) calculations

To explain the experimentally observed different reactivities of **1a** and **2a**, systematic DFT calculations on the reactions of **1a** and **2a** with cyclohexene were investigated. The electronic structures of **1a** and **2a** were calculated at the B3LYP/Def2-TZVPP//B3LYP/Def2-SVP level. Both species have a triplet $S = 1$ ground spin state (Table S2†), which is experimentally supported.[22] Interestingly, we find that changing the substituents on the porphyrin ring does not affect the Fe–O bond distance (1.63 Å in both **1a** and **2a**) or Fe–N bond distance (2.03 Å in both **1a** and **2a**) for the triplet species, even though a slight difference is found for the Fe–Cl distance, of 2.45 and 2.52 Å in **1a** and **2a**, respectively (Table S3†). The same Fe–O bond distance in these two species is consistent with the almost equal stretching vibration frequencies of the Fe–O bond obtained from the rRaman experiment, of 829 and 828 cm^{-1} for **1a** and **2a**, respectively (*vide supra*). For both **1a** and **2a**, the lowest excited state is a singlet state, which is higher in energy than the triplet ground state by *ca.* 9 kcal mol^{-1}. The second excited state is a quintet state, which lies *ca.* 13 kcal mol^{-1} higher in energy than the triplet ground state. Thus, these two excited states have been considered in the following reactivity study; the septet state with an electronic configuration of either d_{xy}^1, $\pi^*_{xz}{}^1$, $\pi^*_{yz}{}^1$, $\sigma^*_{x^2-y^2}{}^1$, $\sigma^*_{z^2}{}^1$, $a_{2u}{}^1$ or d_{xy}^1, $\pi^*_{xz}{}^1$, $\pi^*_{yz}{}^1$, $\sigma^*_{x^2-y^2}{}^1$, $\sigma^*_{z^2}{}^0$, $a_{2u}{}^1$, $e_{2g}{}^1$ was too high in energy to be considered feasible. Given the difference in the oxidation reactivities determined by the experiments, the apparent lack of differences between triplet **1a** and **2a** was puzzling. To further explain the reactivity differences between these two $Fe^{IV}O$ species, we investigated their oxidation reactions using the DFT approach. In the present work, we studied two possible electron transfer pathways, a σ pathway and a π pathway (Fig. 6), for both hydroxylation and epoxidation reactions on both triplet and quintet state surfaces. In the case of the σ pathway, an α-electron is transferred from the substrate bonding orbital to the $\sigma^*_{z^2}$ orbital of the catalyst. In the case of the π pathway, a β-electron is transferred from the

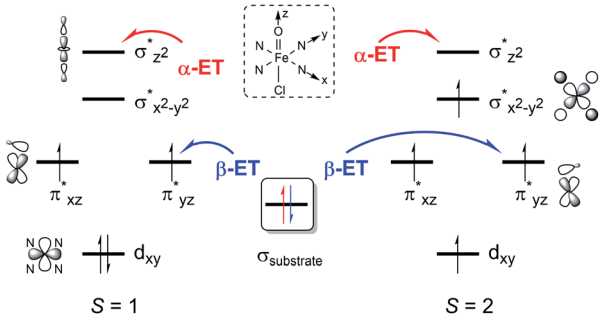

Fig. 6 Two possible electron transfer pathways (α-ET *vs.* β-ET) on both triplet ($S = 1$) and quintet ($S = 2$) spin state surfaces during cyclohexene oxidation by **1a** and **2a**.

substrate to the π^*_{yz} orbital of the catalyst (the *y*-direction here is understood as the direction forming an O–H bond). For the same reaction on the singlet state surface, only a π pathway with an α-electron being transferred from the substrate to the π^*_{yz} orbital of the catalyst was studied (Fig. S20†).

Reactivity study for 1a. Calculation results reveal that both the C–H bond hydroxylation and C=C bond epoxidation reactions mediated by **1a** should occur mainly on the $S = 1$ ground spin state surface. Therein, the C–H bond hydroxylation has a lowest energy barrier of 19.7 kcal mol^{-1} (Fig. 7), which is very close to the experimental value of 20.2 kcal mol^{-1} obtained from $k_{2(H)}$ of 6.1 × 10^{-3} M^{-1} s^{-1} at 283 K using the Eyring equation. In contrast, the C=C bond epoxidation affords a lowest energy barrier of 23.7 kcal mol^{-1}, which indicates that this is an impossible reaction route. These computational results are in accordance with the experimental findings discussed above, in which the hydroxylation product was found to be the sole product. After inspecting the spin density populations along the reaction coordinate on the triplet state surface (Table S4†), it is observed that a β-electron has been transferred from the substrate to the catalyst during the C–H bond reaction, affording the lowest transition state, $^{3\beta}$**TS**$_H$. After the initial $^{3\beta}$**TS**$_H$, an intermediate ($^{3\beta}$**IM**$_H$) with a doublet Fe(III)–OH ferromagnetically coupled to a doublet cyclohexenyl radical was obtained. Compared to other possible reaction routes, this one is both kinetically and thermodynamically favorable (Fig. 7).

Reactivity study for 2a. Then, the same reactivity studies were carried out for **2a**. Even though neither C–H bond hydroxylation nor C=C bond epoxidation of cyclohexene by **2a** can take place easily as a consequence of the very high reaction energy barriers (Fig. 8), C–H bond hydroxylation with a smaller energy barrier of 21.7 kcal mol^{-1} is still preferred to C=C bond epoxidation with a higher energy barrier of 25.8 kcal mol^{-1}. This is also supported by the experiment performed in the presence of a base, in which **2a** was considered to react with the substrate directly (*vide supra*). Thus, the reactions of both **1a** and **2a** with cyclohexene should lead to the hydroxylation product being obtained as the sole product, which is similar to the previous findings for nonheme iron(IV)-oxo cases.[10d,e] In contrast, without adding a base, an epoxide product was observed as the sole product instead in the reaction of **2a** and cyclohexene, which is different from that with a base. Combined with the experimental findings shown above, **2a** can be excluded as the real intermediate that completes the substrate oxidation in the absence of a base.

Disproportionation reaction. According to the current experimental results and previous reports,[4,19–21] an Fe^{IV}O porphyrin π-cation radical species generated from the disproportionation of an Fe^{IV}O intermediate is believed to be the real oxidant to complete the substrate oxidation in the TMP (*i.e.*, **2a**) case. The thermodynamics of this disproportionation process were therefore studied for both **1a** and **2a** cases (Table 2). Three cases were studied: disproportionation of (i) two Fe^{IV}O intermediates (**1a** or **2a**), forming Fe^{III}O and **1b** or **2b**, (ii) protonated **1a** or **2a** with **1a** or **2a** forming Fe^{III}OH and **1b** or **2b** and (iii) two protonated **1a** or **2a** forming Fe^{III}OH$_2$ and **1b** or **2b**. Case (i) was found to be thermodynamically impossible, while case (iii), which would fit a scenario where the proton availability is abundant, would have resulted in a non-rate-limiting activation barrier for the disproportionation, which should then have led to reaction rates comparable to pure **1b** and **2b** (Table 2). Therefore, case (ii), which fits a scenario where limited protons are available, gives the best agreement with the current experimental results. It supports the disproportionation reaction in the case of **2a**, whereas endothermicity makes disproportionation less likely in the case of **1a**. This can be attributed to the higher electron-donating ability of the substituent in TMP, which should make the disproportionation reaction thermodynamically more favourable.[19a] The estimated upper energy barrier for the disproportionation reaction of **2a** is the same as the hydroxylation barrier of cyclohexene. Furthermore, the need for protons to facilitate the disproportionation reaction of the Fe(IV)(O) species has also been previously documented.[4,19a,20]

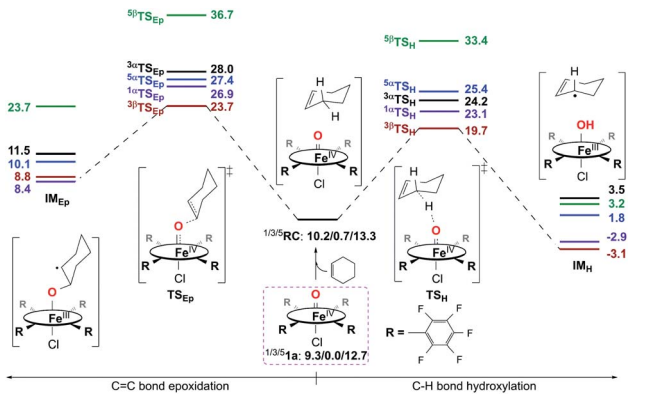

Fig. 7 Energy profiles (in kcal mol^{-1}) calculated at the B3LYP/Def2-TZVPP//Def2-SVP level for the oxidation of cyclohexene by **1a**. α/β in the superscript represents an α/β-electron transferring from substrate to catalyst during the first step of the reaction. RC is a reactant complex, TS is a transition state, and IM is an intermediate species.

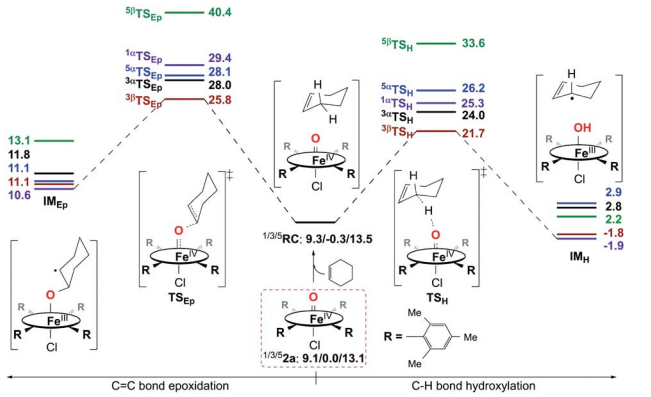

Fig. 8 Energy profiles (in kcal mol^{-1}) calculated at the B3LYP/Def2-TZVPP//Def2-SVP level for the oxidation of cyclohexene by **2a**. α/β in the superscript represents an α/β-electron transferring from substrate to catalyst during the first step of the reaction. RC is a reactant complex, TS is a transition state, and IM is an intermediate species.

Table 2 Thermodynamics of the disproportionation reactions of **1a** and **2a**

	ΔE (kcal mol^{-1})	
Reaction	**1a**	**2a**
$Fe^{IV}(O)(L) + Fe^{IV}(O)(L) \rightarrow Fe^{IV}(O)(L^{+\bullet}) + Fe^{III}(O)(L)$	55.5	51.5
$Fe^{IV}(OH)(L) + Fe^{IV}(O)(L) \rightarrow Fe^{IV}(O)(L^{+\bullet}) + Fe^{III}(OH)(L)$	7.18	−1.87
$Fe^{IV}(OH)(L) + Fe^{IV}(OH)(L) \rightarrow Fe^{IV}(O)(L^{+\bullet}) + Fe^{III}(OH_2)(L)$	−1.04	−12.0

Reactivity study for 1b. The reaction of **1b** with cyclohexene afforded a lowest energy barrier of 8.4 kcal mol^{-1} (Table S5†), which reproduces the experimental value of 8.3 kcal mol^{-1}, obtained from k_2 of 1.4 × 10^4 M^{-1} s^{-1} at 213 K (Table 1) using the Eyring equation. This reaction is the epoxidation on the doublet spin state surface, which is also in agreement with the experimental KIE result of 1.0 as well as the epoxide product distribution.

Reactivity study for 2b. A theoretical study investigating the reaction of **2b** with cyclohexene has been done previously, using a slightly different basis set.[11c] According to those results, the epoxidation pathway should be preferred under the present experimental conditions, which is in good agreement with the current experimental findings. This result therefore confirms that a disproportionation reaction in the **2a** case must occur; otherwise, a C–H bond hydroxylation product should have been seen.

Comparison between 1b and 2b. To make a comparison between **1b** and **2b**, single-point calculations using the same method as in the **1b** case were carried out on the previously optimized geometries in the reaction of **2b** and cyclohexene (Fig. 9).[11c] The lowest energy barrier obtained was 12.9 kcal mol^{-1} (Fig. 9 and Table S5†), which is close to the experimental value of 13.6 kcal mol^{-1} obtained from k_{ox} of 21 M^{-1} s^{-1} at 253 K (Table 1) using the Eyring equation. The epoxidation reaction route is preferred in both **1b** and **2b** cases, which is also similar to previous findings for nonheme iron(v)-oxo cases.[10d,e] **1b** presents a higher oxidation capability than **2b** (Table S5†),[12d] which is consistent with the experiments. Furthermore, the good agreement between theory and experiment in turn demonstrates the accuracy and reliability of the DFT results discussed above.

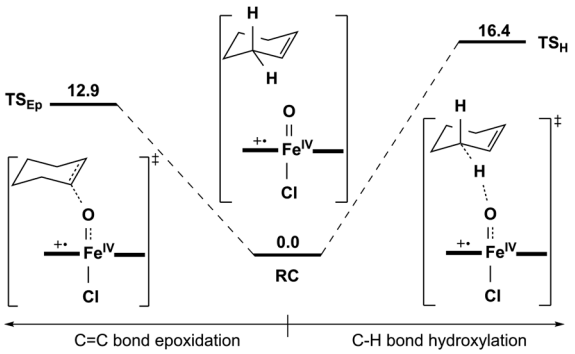

Fig. 9 Energy profiles (in kcal mol^{-1}) calculated at the B3LYP/Def2-TZVPP//LACVP level of two lowest transition states for the oxidation of cyclohexene by **2b**. RC is the reactant complex. TS is the transition state.

Conclusion

In summary, the present study provides valuable mechanistic insights into the chemical properties of heme Cpd II models, such as the chemoselectivity of iron(IV)-oxo porphyrin complexes, which varies depending on the electron-richness of porphyrin ligands. That is, in the oxidation of cyclohexene, a high-valent iron(IV)-oxo complex bearing an electron-deficient porphyrin ligand, $[Fe^{IV}(O)(TPFPP)(Cl)]^-$ (**1a**), prefers allylic C–H bond hydroxylation with a high KIE of 41, yielding 2-cyclohexen-1-ol as the product, whereas a high-valent iron(IV)-oxo complex bearing an electron-rich porphyrin ligand, $[Fe^{IV}(O)(TMP)(Cl)]^-$ (**2a**), favors C=C bond epoxidation to afford the cyclohexene oxide product with a KIE of 1. The latter result is rationalized with the disproportionation of **2a**, resulting in the generation of $[Fe^{IV}(O)(TMP^{+\bullet})]^+$ (**2b**) as the active oxidant that effects the cyclohexene epoxidation. In the presence of a base, this disproportionation reaction is prohibited and the cyclohexene oxidation by **2a** occurs *via* C–H bond hydroxylation to yield 2-cyclohexen-1-ol as the product. Thus, based on experimental and theoretical investigations, we conclude that the chemoselectivity of heme Cpd II models is the same as that of nonheme iron(IV)-oxo species and C–H bond hydroxylation is preferred to the C=C bond epoxidation pathway in the oxidation of cyclohexene.

We have also shown that the disproportionation of heme Cpd II models depends on the electron-richness of the iron(IV)-oxo porphyrin complexes. That is, an electron-deficient iron(IV)-oxo porphyrin complex is difficult to disproportionate, whereas an electron-rich iron(IV)-oxo porphyrin complex readily disproportionates to form Cpd I as an active oxidant. The disproportionation reaction is shown to be affected by the presence of acid or base. Thus, we conclude that care should be taken in investigating the chemical properties of heme Cpd II models because of the possible involvement of the disproportionation of Cpd II to Cpd I, and Cpd I becoming the actual intermediate for the oxidation of organic substrates.

Data availability

All data (experimental and theoretical details) required to understand and verify the research in this article have been provided as the ESI† in the online version of the article at the publisher's website.

Author contributions

Wonwoo Nam conceived and designed the experiments; Ranjana Gupta, Mi Sook Seo, and Ritimukta Sarangi performed the experiments; Xiao-Xi Li and Youngseob Lee performed the theoretical calculation (DFT); Yong-Min Lee, Ranjana Gupta, Xiao-Xi Li, Mi Sook Seo, Sachiko Yanagisawa, Minoru Kubo,

Ritimukta Sarangi, and Kyung-Bin Cho analysed the data; Wonwoo Nam, Shunichi Fukuzumi, Kyung-Bin Cho, Ritimukta Sarangi, and Yong-Min Lee co-wrote the manuscript.

Conflicts of interest

There are no conflicts to declare.

Acknowledgements

This work was supported by the NRF of Korea through CRI (NRF-2021R1A3B1076539 to W. N.) and Basic Science Research Program (NRF-2020R1I1A1A01074630 to Y.-M. L., NRF-2019R1I1A1A01055822 to M. S. S. and NRF-2021R1A2C1012851 to K.-B. C.). The SSRL Structural Molecular Biology Program is supported by the DOE Office of Biological and Environmental Research, and by the National Institutes of Health, National Institute of General Medical Sciences (P30GM133894).

Notes and references

1 (*a*) K. D. Dubey and S. Shaik, *Acc. Chem. Res.*, 2019, **52**, 389–399; (*b*) P. C. E. Moody and E. L. Raven, *Acc. Chem. Res.*, 2018, **51**, 427–435; (*c*) F. P. Guengerich, *ACS Catal.*, 2018, **8**, 10964–10976; (*d*) C. M. Krest, E. L. Onderko, T. H. Yosca, J. C. Calixto, R. F. Karp, J. Livada, J. Rittle and M. T. Green, *J. Biol. Chem.*, 2013, **288**, 17074–17081; (*e*) P. R. Ortiz de Montellano, *Chem. Rev.*, 2010, **110**, 932–948.

2 (*a*) M. Guo, T. Corona, K. Ray and W. Nam, *ACS Cent. Sci.*, 2019, **5**, 13–28; (*b*) J. J. D. Sacramento and D. P. Goldberg, *Acc. Chem. Res.*, 2018, **51**, 2641–2652; (*c*) X. Huang and J. T. Groves, *Chem. Rev.*, 2018, **118**, 2491–2553; (*d*) R. A. Baglia, J. P. T. Zaragoza and D. P. Goldberg, *Chem. Rev.*, 2017, **117**, 13320–13352.

3 (*a*) A. P. Ledray, C. M. Krest, T. H. Yosca, K. Mittra and M. T. Green, *J. Am. Chem. Soc.*, 2020, **142**, 20419–20425; (*b*) K. Mittra and M. T. Green, *J. Am. Chem. Soc.*, 2019, **141**, 5504–5510; (*c*) Y. J. Jeong, Y. Kang, A.-R. Han, Y.-M. Lee, H. Kotani, S. Fukuzumi and W. Nam, *Angew. Chem., Int. Ed.*, 2008, **47**, 7321–7324; (*d*) R. van Eldik, *Coord. Chem. Rev.*, 2007, **251**, 1649–1662; (*e*) W. Nam, S.-E. Park, I. K. Lim, M. H. Lim, J. Hong and J. Kim, *J. Am. Chem. Soc.*, 2003, **125**, 14674–14675.

4 K. Nishikawa, Y. Honda and H. Fujii, *J. Am. Chem. Soc.*, 2020, **142**, 4980–4984.

5 (*a*) S. Kal and L. Que Jr, *J. Biol. Inorg. Chem.*, 2017, **22**, 339–365; (*b*) E. I. Solomon, S. Goudarzi and K. D. Sutherlin, *Biochemistry*, 2016, **55**, 6363–6374; (*c*) E. G. Kovaleva and J. D. Lipscomb, *Nat. Chem. Biol.*, 2008, **4**, 186–193; (*d*) C. Krebs, D. Galonić Fujimori, C. T. Walsh and J. M. Bollinger Jr, *Acc. Chem. Res.*, 2007, **40**, 484–492.

6 J.-U. Rohde, J.-H. In, M. H. Lim, W. W. Brennessel, M. R. Bukowski, A. Stubna, E. Münck, W. Nam and L. Que Jr, *Science*, 2003, **299**, 1037–1039.

7 (*a*) V. A. Larson, B. Battistella, K. Ray, N. Lehnert and W. Nam, *Nat. Rev. Chem.*, 2020, **4**, 404–419; (*b*) X. Engelmann, I. Monte-Pérez and K. Ray, *Angew. Chem., Int. Ed.*, 2016, **55**, 7632–7649; (*c*) S. A. Cook and A. S. Borovik, *Acc. Chem. Res.*, 2015, **48**, 2407–2414; (*d*) W. Nam, *Acc. Chem. Res.*, 2015, **48**, 2415–2423; (*e*) M. Puri and L. Que Jr, *Acc. Chem. Res.*, 2015, **48**, 2443–2452; (*f*) W. Nam, Y.-M. Lee and S. Fukuzumi, *Acc. Chem. Res.*, 2014, **47**, 1146–1154.

8 (*a*) M. S. Seo, N. H. Kim, K.-B. Cho, J. E. So, S. K. Park, M. Clémancey, R. Garcia-Serres, J.-M. Latour, S. Shaik and W. Nam, *Chem. Sci.*, 2011, **2**, 1039–1045; (*b*) A. N. Biswas, M. Puri, K. K. Meier, W. N. Oloo, G. T. Rohde, E. L. Bominaar, E. Münck and L. Que Jr, *J. Am. Chem. Soc.*, 2015, **137**, 2428–2431; (*c*) I. Monte-Pérez, X. Engelmann, Y.-M. Lee, M. Yoo, E. Kumaran, E. R. Farquhar, E. Bill, J. England, W. Nam, M. Swart and K. Ray, *Angew. Chem., Int. Ed.*, 2017, **56**, 14384–14388.

9 K.-B. Cho, H. Hirao, S. Shaik and W. Nam, *Chem. Soc. Rev.*, 2016, **45**, 1197–1210.

10 (*a*) Y. H. Kwon, B. K. Mai, Y.-M. Lee, S. N. Dhuri, D. Mandal, K.-B. Cho, Y. Kim, S. Shaik and W. Nam, *J. Phys. Chem. Lett.*, 2015, **6**, 1472–1476; (*b*) S. N. Dhuri, K.-B. Cho, Y.-M. Lee, S. Y. Shin, J. H. Kim, D. Mandal, S. Shaik and W. Nam, *J. Am. Chem. Soc.*, 2015, **137**, 8623–8632; (*c*) S. Kim, K.-B. Cho, Y.-M. Lee, J. Chen, S. Fukuzumi and W. Nam, *J. Am. Chem. Soc.*, 2016, **138**, 10654–10663; (*d*) W. N. Oloo, Y. Feng, S. Iyer, S. Parmelee, G. Xue and L. Que Jr, *New J. Chem.*, 2013, **37**, 3411–3415; (*e*) V. Dantignana, J. Serrano-Plana, A. Draksharapu, C. Magallón, S. Banerjee, R. Fan, I. Gamba, Y. Guo, L. Que Jr, M. Costas and A. Company, *J. Am. Chem. Soc.*, 2019, **141**, 15078–15091; (*f*) X.-X. Li, K.-B. Cho and W. Nam, *Bull. Korean Chem. Soc.*, 2021, **42**, 1506–1512.

11 (*a*) W. J. Song, Y. O. Ryu, R. Song and W. Nam, *J. Biol. Inorg. Chem.*, 2005, **10**, 294–304; (*b*) A.-R. Han, Y. J. Jeong, Y. Kang, J. Y. Lee, M. S. Seo and W. Nam, *Chem. Commun.*, 2008, 1076–1078; (*c*) R. Gupta, X.-X. Li, K.-B. Cho, M. Guo, Y.-M. Lee, Y. Wang, S. Fukuzumi and W. Nam, *J. Phys. Chem. Lett.*, 2017, **8**, 1557–1561.

12 (*a*) H. Fujii, *J. Am. Chem. Soc.*, 1993, **115**, 4641–4648; (*b*) H. Fujii, *Coord. Chem. Rev.*, 2002, **226**, 51–60; (*c*) M. Asaka and H. Fujii, *J. Am. Chem. Soc.*, 2016, **138**, 8048–8051; (*d*) Y. Ishimizu, Z. Ma, M. Hada and H. Fujii, *J. Biol. Inorg. Chem.*, 2019, **24**, 483–494; (*e*) N. Fukui, K. Ueno, M. Hada and H. Fujii, *Inorg. Chem.*, 2021, **60**, 3207–3217; (*f*) Y. Suzuki, M. Hada and H. Fujii, *J. Inorg. Biochem.*, 2021, **223**, 111542; (*g*) K. Ueno, Y. Ishimizu and H. Fujii, *Inorg. Chem.*, 2021, **60**, 9243–9247; (*h*) Y. Ishimizu, Z. Ma, M. Hada and H. Fujii, *Inorg. Chem.*, 2021, **60**, 17687–17698.

13 (*a*) Y. M. Goh and W. Nam, *Inorg. Chem.*, 1999, **38**, 914–920; (*b*) D. Kumar, L. Tahsini, S. P. de Visser, H. Y. Kang, S. J. Kim and W. Nam, *J. Phys. Chem. A*, 2009, **113**, 11713–11722.

14 (*a*) T. Kitagawa and Y. Mizutani, *Coord. Chem. Rev.*, 1994, **135/136**, 685–735; (*b*) K. Nakamoto, *Coord. Chem. Rev.*, 2002, **226**, 153–165; (*c*) J. Terner, V. Palaniappan, A. Gold, R. Weiss, M. M. Fitzgerald, A. M. Sullivan and C. M. Hosten, *J. Inorg. Biochem.*, 2006, **100**, 480–501.

15 (*a*) C. V. Sastri, M. J. Park, T. Ohta, T. A. Jackson, A. Stubna, M. S. Seo, J. Lee, J. Kim, T. Kitagawa, E. Münck, L. Que Jr and W. Nam, *J. Am. Chem. Soc.*, 2005, **127**, 12494–12495; (*b*) Y.-M. Lee, S. N. Dhuri, S. C. Sawant, J. Cho, M. Kubo, T. Ogura, S. Fukuzumi and W. Nam, *Angew. Chem., Int. Ed.*, 2009, **48**, 1803–1806; (*c*) S. Hong, H. So, H. Yoon, K.-B. Cho, Y.-M. Lee, S. Fukuzumi and W. Nam, *Dalton Trans.*, 2013, **42**, 7842–7845.

16 (*a*) R. Sarangi, *Coord. Chem. Rev.*, 2013, **257**, 459–472; (*b*) T. E. Westre, P. Kennepohl, J. G. DeWitt, B. Hedman, K. O. Hodgson and E. I. Solomon, *J. Am. Chem. Soc.*, 1997, **119**, 6297–6314.

17 (*a*) T. Kojima, Y. Hirai, T. Ishizuka, Y. Shiota, K. Yoshizawa, K. Ikemura, T. Ogura and S. Fukuzumi, *Angew. Chem., Int. Ed.*, 2010, **49**, 8449–8453; (*b*) J. M. Mayer, *Acc. Chem. Res.*, 2011, **44**, 36–46; (*c*) I. Garcia-Bosch, A. Company, C. W. Cady, S. Styring, W. R. Browne, X. Ribas and M. Costas, *Angew. Chem., Int. Ed.*, 2011, **50**, 5648–5653; (*d*) J. Park, Y.-M. Lee and W. Nam, *J. Am. Chem. Soc.*, 2013, **135**, 5052–5061; (*e*) T. Ishizuka, S. Ohzu, H. Kotani, Y. Shiota, K. Yoshizawa and T. Kojima, *Chem. Sci.*, 2014, **5**, 1429–1436; (*f*) L. Zhang, Y.-M. Lee, M. Guo, S. Fukuzumi and W. Nam, *J. Am. Chem. Soc.*, 2020, **142**, 19879–19884.

18 (*a*) S. Fukuzumi, Y.-M. Lee and W. Nam, *Bull. Korean Chem. Soc.*, 2021, **42**, 1558–1568; (*b*) P. T. Truong, S. G. Miller, E. J. M. S. Maria and M. A. Bowring, *Chem.–Eur. J.*, 2021, **27**, 14800–14815; (*c*) S. Fukuzumi, Y.-M. Lee and W. Nam, *Bull. Korean Chem. Soc.*, 2020, **41**, 1217–1232.

19 (*a*) Z. Pan and M. Newcomb, *Inorg. Chem. Commun.*, 2011, **14**, 968–970; (*b*) R. Zhang and M. Newcomb, *Acc. Chem. Res.*, 2008, **41**, 468–477; (*c*) Z. Pan and M. Newcomb, *Inorg. Chem.*, 2007, **46**, 6767–6774; (*d*) R. Zhang, J. H. Horner and M. Newcomb, *J. Am. Chem. Soc.*, 2005, **127**(18), 6573–6582.

20 (*a*) X. Lu, Y.-M. Lee, M. S. Seo and W. Nam, *Chem. Commun.*, 2020, **56**, 11207–11210; (*b*) S. Fukuzumi, N. Fujioka, H. Kotani, K. Okhubo, Y.-M. Lee and W. Nam, *J. Am. Chem. Soc.*, 2009, **131**, 17127–17134.

21 (*a*) M. Wolak and R. van Eldik, *Chem.–Eur. J.*, 2007, **13**, 4873–4883; (*b*) J. T. Groves, Z. Gross and M. K. Stern, *Inorg. Chem.*, 1994, **33**, 5065–5072.

22 J. T. Groves, R. C. Haushalter, M. Nakamura, T. E. Nemo and B. J. Evans, *J. Am. Chem. Soc.*, 1981, **103**, 2884–2886.